One-Pot Synthesis, Structure, and Unusual Luminescence of Novel One-Dimensional Lanthanide(III) Tetramethoxyborates

Alison S. Gajadhar-Plummer,[†] Ishenkumba A. Kahwa,*[,†] Andrew J. P. White,[‡] and David J. Williams[‡]

Chemistry Department, University of the West Indies, Mona Campus, Kingston 7, Jamaica, and Chemistry Department, Imperial College of Science, Technology and Medicine, South Kensington, London SW7 2AY, United Kingdom

Received September 9, 1998

Detailed studies of formation, structure, and luminescence characteristics of novel ionically linked sinusoidal chains of $[\{Na\}\{(\mathbf{sal})_3Ln(B(OCH_3)_4)Ln(\mathbf{sal})_3\}]_n$ [Ln = Nd, Sm, Tb−Lu, Y (**4**); Ln = Eu (**5**); Ln = Gd (**6**)] was undertaken to assess the versatility of tetramethoxyborate anions as consistent general synthons for one-dimensional materials. Crystal data for $[\{Na\}\{(\mathbf{sal})_3Nd(B(OCH_3)_4)Nd(\mathbf{sal})_3\}]_n$ [**4**(Ln = Nd)]: monoclinic; space group, *C*2/*c* (15), $a = 20.884(2)$ Å, $b = 12.454(1)$ Å, $c = 37.663(5)$ Å, $\beta = 102.09(2)°$, $Z = 8$; $[\{Na\}\{(\mathbf{sal})_3Eu(B(O\,CH_3)_4)Eu(\mathbf{sal})_3\}]_n$ (**5**): monoclinic; space group, *C*2/*c* (15), $a = 20.846(2)$ Å, $b = 12.460(1)$ Å, $c = 37.365(4)$ Å, $\beta = 102.17(1)°$, $Z = 8$. Europium luminescence from $[\{Na\}\{(\mathbf{sal})_3Ln_{1-x}Eu_x(B(OCH_3)_4)Ln_{1-x}Eu_x(\mathbf{sal})_3\}]_n$ [Ln = Eu (**5**); Gd (**7**−**11**), Y (**12**), Dy (**13**−**18**), Dy/Gd (**19**)] reveals the presence of defect Eu^{3+} sites, possibly resulting from swapping regular Eu^{3+} and Na^+ positions. Strong Eu^{3+}−Eu^{3+} electronic interactions result in multidimensional energy migration and a dynamic excitation energy-transport regime. Efficient thermally activated regular Eu^{3+}-to-defect Eu^{3+} back-energy transfer dominates at 297 K.

Introduction

Although simple tetra-alkoxyborate anions ($[(RO)_4B]^-$ R = alkyl group) have been known for about a century,[1] relatively few reports on their coordination behavior exist. Most of the reported examples cover discrete complexes of groups one[2] and two[3] elements for which the bidentate coordination behavior of the $[(RO)_4B]^-$ chelates is prominent. However, the $[(CH_3O)_4B]^-$ anion displays remarkable versatility as a template for metallopolymers of one-dimensional structural motifs. In two separate serendipitous events, large lanthanide(III) ions (Ln = La−Nd), formed linear $[Ln(NO_3)_2((CH_3O)_4B)(CH_3OH)_2]_n$ (**1**)[4] polymers, whereas cadmium(II) formed helical chains of the salt $[Cd(tcm)B(OCH_3)_4]\cdot xCH_3OH$ (tcm = $[C(CN)_3]^-$)[5] (**2**). These broad similarities in structural motifs are observed despite vast differences in the chemical properties of hard lanthanide(III) and soft cadmium(II) Lewis acids. The $[(CH_3O)_4B]^-$ ion and other tetra-alkoxyborates generally are thus attractive as potential synthons in the preparation, and rational crystal engineering, of materials in which strict control of the directionality of physical behavior such as magnetism and magnetic coupling,[6] electron and electronic energy[7] transport, or polarization[8] is desired. The problem is that the conditions under which the above-mentioned one-dimensional arrays are assembled by the tetramethoxyborate anions are enigmatic.

We have been interested in tetra-alkoxyborate and tetraphenoxyborate chelates as preparative templates for one-dimensional lanthanide(III) compounds with electronic energy-transport characteristics that could be readily manipulated. In the presence of efficient light-harvesting chromophores (light antennae),[9] which are coupled to lanthanide(III) electronic states, and are therefore capable of sensitizing intense red europium(III) or green terbium(III) emission, one-dimensional arrays are of great interest in fluorescent sensors[10] and diagnostic[11] applications. After numerous unsuccessful attempts, including one with **3**, we discovered that one-pot methanolysis of boron species generated from Borax ($Na_2[B_4O_5(OH)_4]\cdot 8H_2O$) in the presence of salicylaldehyde (**Hsal**) and neodymium(III) nitrate produces a novel ionicaly linked polymeric sinusoidal one-dimensional $[\{Na\}\{(\mathbf{sal})_3Nd(B(OCH_3)_4)Nd(\mathbf{sal})_3\}]_n$ compound. We have successfully used this technique to prepare complexes of almost the entire lanthanide(III) series ($[\{Na\}\{(\mathbf{sal})_3Ln(B(OCH_3)_4)Ln(\mathbf{sal})_3\}]_n$ [Ln = Nd, Sm, Tb−Lu, Y (**4**); Ln = Eu (**5**); Ln = Gd (**6**)]). To the best of our knowledge, this is the first consistent method for fabricating metallo−one-dimensional arrays using tetra-alkoxyborate synthons. With this breakthrough as well as series **1** and **2**, it seems that design and preparation of

* Correspondence to: Dr. Ishenkumba A. Kahwa, Chemistry Department, University of the West Indies, Mona, Kingston 7, Jamaica. Tel.: (876) 927-1910. Fax: (876) 977-1835. E-mail: ikahwa@uwimona.edu.jm.

† University of the West Indies.

‡ Imperial College of Science, Technology and Medicine.

(1) Copaux, H. *Compt. Rend.* **1898**, *127*, 719.
(2) Al-Juaid, S. S.; Eaborn, C.; El-Kheli, M. N. A.; Hitchcock, P. B.; Lickiss, P. D.; Molla, M. E.; Smith, J. D.; Zora, J. A. *J. Chem. Soc., Dalton Trans.* **1989**, 449.
(3) Lappert, M. F. *Chem. Rev.* **1958**, *56*, 999.
(4) Mathews, K. D.; Kahwa, I. A.; Williams, D. J. *Inorg. Chem.* **1993**, *32*, 1442.
(5) Batten, S. R.; Hoskins, B. F.; Robson, R. *Angew. Chem., Int. Ed. Engl.* **1997**, *36*, 636.
(6) Decurtins, S.; Schmalle, W. H.; Schneuwly, P.; Ensling, J.; Gutlich, P. *J. Am. Chem. Soc.* **1994**, *116*, 9521.
(7) Webber, S. E.; *Chem. Rev.* **1990**, *90*, 1469.
(8) Thalladi, V. R.; Brassele, S., Bläser, D.; Boesse, R.; Zyss, J.; Nangia A.; Desiraju, G. R. *J. Chem. Soc., Chem. Commun.* **1997**, 1841.
(9) (a) Balzani, V.; Scandola, F. *Supramolecular Photochemistry*; Ellis Horwood: Chichester, 1991; Chapter 12. (b) Parker, D.; Williams J. A. G. *J. Chem. Soc., Dalton Trans.* **1996**, 3613.
(10) Richardson, R. S. *Chem. Rev.* **1982**, *82*, 541.
(11) Meares, C. F.; Wensel, T. G. *Acc. Chem. Res.* **1984**, *17*, 7, 202.

10.1021/ic9810788 CCC: $18.00
Published on Web 03/31/1999

Table 1. Numerical Assignments and Stoichiometries for $[\{Na\}\{(sal)_3Ln'_{1-x}Ln_x(B(OMe)_4)Ln'_{1-x}Ln_x(sal)_3\}]_n \cdot mH_2O$ Compounds

compound	$[\{Na\}\{(\mathbf{sal})_3Ln'_{1-x}Ln_x(B(OMe)_4)Ln'_{1-x}Ln_x(\mathbf{sal})_3\}]_n \cdot mH_2O$		
	Ln	Ln′	*x*
4	Nd−Lu, Y	Nd−Lu, Y	
5	Eu	Eu	
6	Gd	Gd	
7	Eu	Gd	0.06
8	Eu	Gd	0.16
9	Eu	Gd	0.37
10	Eu	Gd	0.51
11	Eu	Gd	0.79
12	Eu	Y	0.04
13	Eu	Dy	0.03
14	Eu	Dy	0.09
15	Eu	Dy	0.16
16	Eu	Dy	0.50
17	Eu	Dy	0.58
18	Eu	Dy	0.76
19	Eu	Dy/Gd	≈0.29

structurally diverse one-dimensional arrays using tetra-alkoxyborates is achievable and it is now possible for electronic properties of an extended series of compounds of low dimensionality, such as $[\{Na\}\{(\mathbf{sal})_3Ln(B(OCH_3)_4)Ln(\mathbf{sal})_3\}]_n$, to be evaluated.

Herein, we report the preparation, crystal structure, and intriguing luminescence decay dynamics of the $[\{Na\}\{(\mathbf{sal})_3Ln(B(OCH_3)_4)Ln(\mathbf{sal})_3\}]_n$ series.

Experimental Section

Materials. Salicylaldehyde (99%), standard pH 9.22 buffer tablets, and Borax ($Na_2[B_4O_5(OH)_4]\cdot 8H_2O$) were obtained from BDH. Lanthanide(III) nitrates were obtained by neutralizing the corresponding oxides (Aldrich, 99.99% purity) with nitric acid, followed by evaporation of water to near dryness. Methanol was of reagent grade.

Spectral and Quantitative Analyses. Carbon, hydrogen, and nitrogen analyses were obtained from MEDAC Ltd., Brunel Science Center, Surrey, UK; lanthanide concentrations were obtained by neutron activation analysis at the International Center for Environmental and Nuclear Sciences, University of the West Indies, Jamaica.[12] A Perkin-Elmer 1000 S FT-IR and HP 8451A diode array UV−Visible spectrometers were used to record IR and electronic absorption spectra, respectively. The powder X-ray diffraction analyses were obtained from A Siemens D5000 diffractometer.

Syntheses. Compounds **4**−**19** (Table 1) were prepared using standard pH 9.2 buffer tablets or Borax ($Na_2[B_4O_5(OH)_4]\cdot 8H_2O$), as shown in Scheme 1. Crystals were dried on tissue paper to maintain their crystalline integrity. Analyses[13] showed the crystals to be anhydrous for **4** (Ln = Nd); monohydrates for **4** (Ln = Sm, Tm, Lu) and **5**; dihydrates for **4** (Ln = Tb, Dy, Ho, Yb) and **6**; and trihydrates for **4** (Ln = Y, Er). However, powder X-ray diffraction analyses (Figure 1) show (vide infra) that crystals of **4**−**6** are isomorphous irrespective of the hydration number. Further the luminescence decay kinetic values of terbium and europium samples prepared from CH_3OD/D_2O were similar to those of compounds prepared from CH_3OH, which confirms that the water found in the analyses is crystal rather than coordinated water.

Luminescence Studies. The luminescence and excitation spectra were recorded using an LS5B Perkin-Elmer Fluorescence spectrometer that is essentially similar to the one described earlier.[14] The luminescence decay rates were measured using either our new Continuum Powerlite 8000 YAG laser and a matching ND6000 dye Laser, or a nitrogen dye laser, and an electronic and computational setup that was described previously.[12] The Powerlite 8000 YAG laser generates ca. 1200, 600, and 300 mJ pulses (5−8 ns) at 1064, 532, and 355 nm, respectively, whereas the ND6000 may generate up to 150-mJ pulses with the Rhodamine 6G dye. Indiscriminate excitation of samples was effected at 365 nm whereas selective excitation was achieved using a Rhodamine 6G dye tuned at 572 nm for Eu^{3+} ($^5D_0$) and a coumarin 500 dye tuned at 515−535 nm, depending on temperature, for the Eu^{3+} ($^5D_1$) state. Variable temperature measurements (8−320 K) were done using our new APD Cryogenics Inc. CSW-202 Displex Helium refrigerator system with the sample in contact with cryocon-conducting grease. Excitations using light with a wavelength of 337 nm (from a

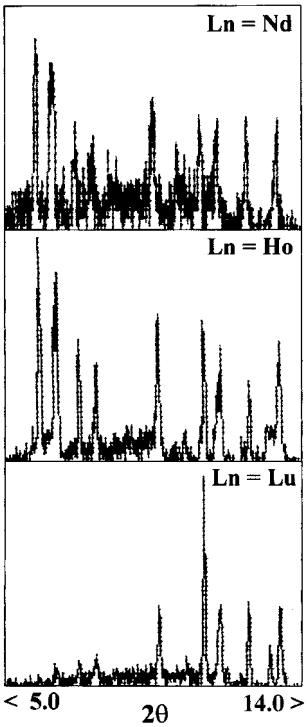

Figure 1. A comparison of powder X-ray diffraction spectra of $[\{Na\}\{(sal)_3Ln(B(OMe)_4)Ln(sal)_3\}]_n$ (**4**) (Ln = Nd, Ho, and Lu).

Scheme 1. Synthesis of $[\{Na\}\{(\mathbf{sal})_3Ln(B(OMe)_4)Ln(\mathbf{sal})_3\}]_n$ (**4**) (Ln = Nd−Lu, Y)

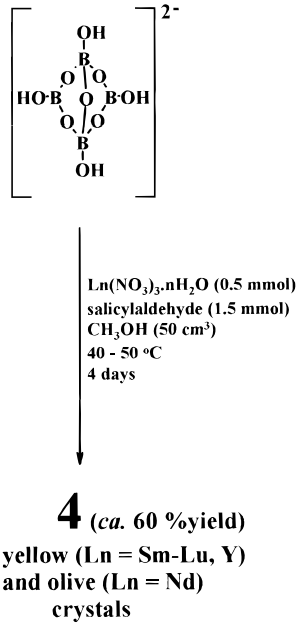

(12) Mathews, K. D.; Fairman, R. A.; Johnson, A.; Spence, K. V. N., Kahwa, I. A.; McPherson, G. L.; Robotham, H. J. *J. Chem. Soc., Dalton Trans.* **1993**, 1719.

(13) Satisfactory analytical data [±0.3% for C, H, and metal (Eu and Dy) analyses] were reported for all compounds. See Supporting Information.

(14) Mathews, K. D.; Kahwa, I. A.; Williams, D. J. *Inorg. Chem.* **1994**, *33*, 1382.

Table 2. Crystallographic Data for $[\{Na\}\{(sal)_3Ln(B(OMe)_4Ln(sal)_3\}]_n$[a]

data	**5**	**4** [Ln = Nd]
formula	$C_{46}H_{42}O_{16}BNaEu_2$	$C_{46}H_{42}O_{16}BNaNd_2$
formula weight	1188.5	1173.1
color, habit	yellow prisms	pale olive prisms
crystal size, mm	0.40 × 0.33 × 0.13	0.37 × 0.20 × 0.17
T, K	293	293
diffractometer	Siemens P4/PC	Siemens P4/PC
wavelength, Å	0.71073	0.71073
lattice type	monoclinic	monoclinic
space group	*C*2/*c*, 15	*C*2/*c*, 15
cell dimensions		
a, Å	20.846(2)	20.884(2)
b, Å	12.460(1)	12.454(1)
c, Å	37.365(4)	37.663(5)
β, deg	102.17(1)	102.09(2)
V, Å^3	9487(2)	9579(2)
Z	8	8
D_c, g cm^{-3}	1.664	1.627
F(000)	4704	4656
μ, cm^{-1}	0.270	0.222
θ range, deg	1.9−25.0	1.9−25.0
no. of unique reflections measured	8364	8456
observed, $\|F_o\| > 4\sigma(\|F_o\|)$	6109	5873
absorption correction	semiempirical (ψ-scans)	semiempirical (ψ-scans)
maximum, minimum transmission	0.21, 0.14	0.40, 0.38
no. of variables	597	597
R_1[b]	0.050	0.053
wR_2[c]	0.099	0.101
weighting factors a, b[d]	0.036, 9.127	0.026, 0.000
largest difference peak, hole, eÅ^{-3}	0.85, −0.61	0.50, −0.47

[a] Details in common: ω-scans, refinement based on F^2. [b] $R_1 = \sum||F_o| - |F_c||/\sum|F_o|$. [c] $wR_2 = \sqrt{\{\sum[w(F_o^2 - F_c^2)^2]/\sum[w(F_o^2)^2]\}}$. [d] $w^{-1} = \sigma^2(F_o^2) + (aP)^2 + bP$.

nitrogen laser) or 282 nm (from the frequency-doubled Rhodamine 6G dye laser) lead to degradation of the samples. Samples were thus routinely inspected for visible damage during the analyses, and duplicate runs were done for most of the luminescence decay curves to ensure reproducibility of decay behavior.

Structure Determination. Table 2 provides a summary of the crystal data, data collection, and refinement parameters for neodymium [**4**(Ln = Nd)] and europium (**5**) compounds. The structures were solved by direct methods and all the nonhydrogen atoms were refined anisotropically using full-matrix least-squares based on F^2. The hydrogen atoms of the methoxy groups were located from ΔF maps and their positions optimized. The remaining hydrogen atoms were placed in calculated positions, and all the hydrogen atoms were assigned isotropic thermal parameters, $U(H) = 1.2\ U_{eq}(C)$ [$U(H) = 1.5\ U_{eq}$(C-Me)], and allowed to ride on their parent atoms. Computations were carried out using the SHELXTL PC program system.[15]

Results and Discussion

Syntheses and Structure. The successful preparation of members of series **4**−**6** is indicated by satisfactory elemental analyses[13] and IR spectra, which show the presence of the carbonyl group (1634 cm^{-1}). The compounds have similar crystal morphologies. This feature together with the similarity in the powder X-ray diffraction patterns of the neodymium and holmium compounds (Figure 1) is indicative of their isomorphic nature. However, the spectrum of the lutetium compound (Figure 1), although it is qualitatively similar to those of the neodymium and holmium compounds, lacks the strong diffracting behavior at low θ. This may indicate some subtle changes in the detailed crystal structure as a result of the lanthanide contraction. Thus single-crystal X-ray diffraction analyses of both the neodymium−holmium and erbium−lutetium complexes are necessary to provide firm evidence for the nature of members of series **4**. Indeed single-crystal X-ray diffraction studies of the neodymium(III) and europium(III) products confirm the formulation of the compounds as $[\{Na\}\{(\mathbf{sal})_3Ln(B(OMe)_4)Ln(\mathbf{sal})_3\}]_n$ as well as their one-dimensional structural motif (Figures 2 and 3).

The X-ray analyses of the neodymium(III) [**4** (Ln = Nd)] and europium(III) (**5**) complexes shows that they are isomorphous (Tables 2 and 3), with only very minor differences in their comparative geometries reflecting the normal lanthanide(III) contraction effects. The structures are ionically linked polymers and contain two independent lanthanide centers. Each of these centers is coordinated to three planar bidentate **sal**$^-$ chelates, the remaining two coordination sites in each case being occupied by a bridging tetramethoxyborate. The geometry at each lanthanide center is slightly distorted square antiprismatic; the principle distortion is an O(2)−Ln−O(3) angle of 58.3(2)° (Ln = Eu) [53.2(2)°, Ln = Nd] as a consequence of the bite of the tetramethoxyborate. The Ln−O coordination distances fall into two distinct groups. The coordination distances of the phenolate oxygen atoms [ranging between 2.286(7) and 2.340(6) Å, Ln = Nd] are, as expected,[16] significantly shorter than those of either the carbonyl [range, 2.397(6)−2.466(7), Ln = Eu; 2.437(6)−2.522(8), Ln = Nd] or tetramethoxyborate oxygens [2.424(6)−2.457(5), Ln = Eu; 2.461(7)−2.502(6), Ln = Nd]. In all cases, the carbonyl groups substantially retain their double-bond character,[16] the C=O distances being in the ranges 1.22(1)−1.24(1) Å (Ln = Eu) and 1.20(1)−1.24(1) Å (Ln = Nd). Likewise, the C−O (phenolate) bonds exhibit a characteristic slight shortening,[16] the C−O distances being in the ranges 1.29(1)−1.30(1) Å (Ln = Eu) and 1.28(1)−1.34(1) Å (Ln = Nd). The bridging tetramethoxyborate ligands show marked departures from T_d geometry, the O−B−O angles ranging between 98.3(7) and 117.2(8)° (Ln = Eu) and between 98.6(7) and 117.0(8) (Ln = Nd). These distortions are similar to those observed in the linear $[La(NO_3)_2(B(OCH_3)_4)(CH_3OH)_2]_n$ system.[4]

Each of the tetramethoxyborate-bridged ($[(\mathbf{sal})_3Ln(B(OMe)_4)Ln(\mathbf{sal})_3]^-$) 'dimers' has approximate C_2 symmetry, virtually down the molecular C_2 axis, as shown in Figure 2. The three phenolate oxygen atoms on each center are directed outward, away from the bridging tetramethoxyborates, thereby presenting a suitable charged binding site for the sodium cations. Indeed, pairs of $[(\mathbf{sal})_3Ln(B(OMe)_4)Ln(\mathbf{sal})_3]^-$ dimers are linked via the sodium cation to form sinusoidal ionically linked polymeric chains (Figure 3) that extend in the crystallographic *c*-direction. The two linking sodium cations are nonequivalent, Na(1) positioned on a crystallographic inversion center and Na(2) on a 2-fold axis.

The intrachain Ln...Ln separations are (given to 2 decimal points to highlight the magnitude of their differences) 6.23 Å, Ln = Eu (6.31 Å, Ln = Nd) within each dimer, and 6.57, 6.84 Å, Ln = Eu (6.61, 6.88 Å, Ln = Nd), respectively, across the linking Na^+ centers. These distances are all shorter than any of the interchain Ln....Ln distances, the shortest of which is 7.22 Å, Ln = Eu (7.28 Å, Ln = Nd), for the Ln(1)....Ln(1) separation. The polymer chains are closely packed with the crests of one

(15) Sheldrick, G. M. *SHELXTL PC*, version 5.03; Siemens Analytical X-ray Instruments Inc.: Madison, WI, 1994.

(16) (a) Kahwa, I. A.; Fronczek, F. R.; Selbin, J. *Inorg. Chim. Acta* **1987**, *126*, 227. (b) Kahwa, I. A.; Fronczek, F. R.; Selbin, J. *Inorg. Chim. Acta* **1988**, *148*, 27.

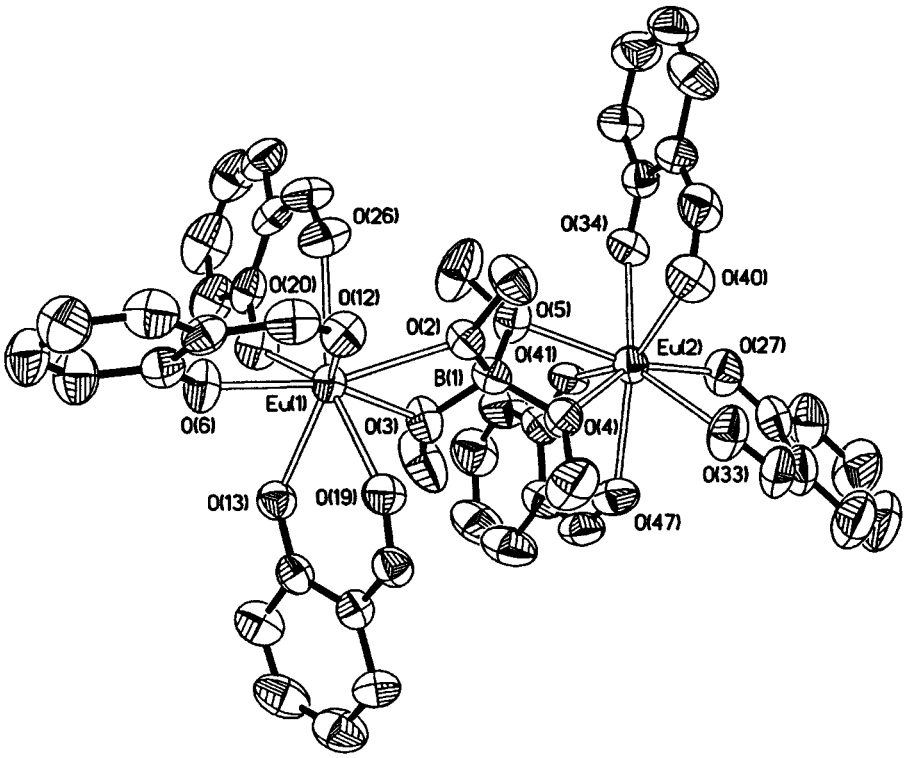

Figure 2. ORTEP diagram of the $[(\mathbf{sal})_3Eu(B(OMe)_4)Eu(\mathbf{sal})_3]^-$ anion showing 50% probability thermal ellipsoids for all nonhydrogen atoms.

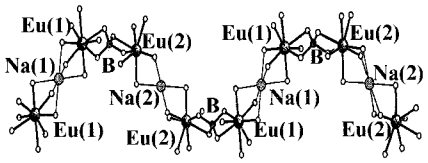

Figure 3. The one-dimensional sinusoidal motif of the $[\{Na\}\{(sal)_3Ln(B(OMe)_4)Ln(sal)_3\}]_n$ ionically linked polymeric chain. Hydrogen and carbon atoms have been omitted for clarity.

chain lying in the troughs of the next. There is no solvent included in the structures of **4**(Ln = Nd) and **5**.

Although the common synthetic route to complexes of $[(RO)_4B]^-$ with groups 1 and 2 metal ions has been via the reaction of $(RO)_3B$ with the RO^- anion under strict exclusion of moisture and air,[2,3] methanolysis of commonly used reagents such as sodium tetrahydroborate and trihydrocyanoborate (leading to **1**),[4] tetraphenylborate (resulting in **2**),[5] and in this study, Borax, seems to proceed well without those limitations.

Series **1** was obtained in a mixture with amino−imino products but attempts to obtain pure products of the series or complexes of smaller lanthanides (Ln = Sm−Lu, Y) failed.[4] In sharp contrast, the formation of **4** with Ln = large lanthanides (La and Pr) seems unfavorable, whereas compounds of the smaller Nd^{3+}−Lu^{3+} are readily obtained. This preference for smaller Ln^{3+} ions by system **4** was revealed conclusively by the mixed lanthanide(III) complexes, $([\{Na\}\{(\mathbf{sal})_3Ln_{1-x}Eu_x(B(OMe)_4)Ln_{1-x}Eu_x(\mathbf{sal})_3\}]_n$ [x = 1 (**5**); Ln = Gd (**6**−**10**), Y (**12**) or Dy (**13**−**18**)], the metal contents of which were established by nuclear activation analyses.[12] The higher selectivity for incorporation of the smaller dysprosium(III) ions (1.03 Å for 8-fold coordination[17]) in crystalline compounds $[\{Na\}\{(\mathbf{sal})_3Dy_{1-x}Eu_x(B(OMe)_4)Dy_{1-x}Eu_x(\mathbf{sal})_3\}]_n$ over the significantly larger europium(III) (1.07 Å) is evident from the cation discrimination index[18] of $I_D \approx 1.3$ (Figure 4). For system

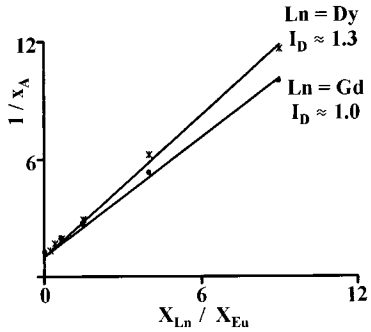

Figure 4. Cation discrimination indices for crystalline $([\{Na\}\{(\mathbf{sal})_3Ln_{1-x}Eu_x(B(OMe)_4)Ln_{1-x}Eu_x(\mathbf{sal})_3\}]_n$ complexes [Ln = Gd (**6**−**10**) or Dy (**13**−**18**)].

$[\{Na\}\{(\mathbf{sal})_3Gd_{1-x}Eu_x(B(OMe)_4)Gd_{1-x}Eu_x(\mathbf{sal})_3\}]_n$, in which Gd^{3+} and Eu^{3+} have more similar ionic radii (1.06 Å for Gd^{3+} in 8-fold coordination[17]) the cation discrimination index accordingly is $I_D \approx 1$ (Figure 4). Further, lanthanide(III) ions have been complexed with tetrahydroborate anion $[H_4B]^-$ numerous times in the presence of CH_3O^- anions. Although some limited methanolysis of the tetrahydroborate anion was reported, no lanthanide(III) compounds of the $[(CH_3O)_4B]^-$ anion or its

(17) Shannon, R. D.; Prewitt, C. T. *Acta Crystallogr.* **1971**, *B25*, 925.

(18) Competitive incorporation of two lanthanide(III) metal ions (A and B) in a mixed crystalline product can be expressed in terms of their respective selectivities:[12]

$$x_A = (X_A P_A)/(X_A P_A + X_B P_B); \quad x_B = (X_B P_B)/(X_A P_A + X_B P_B) \quad (1)$$

where X_A and X_B are the initial mole fractions of cations A and B, respectively, in the mother-reaction mixture; x_A and x_B are mole fractions of cations A and B in the crystalline product, respectively; P_A and P_B are probabilities for the incorporation of cations A and B, respectively, in the crystalline product. For comparative purposes, we set cation A = Eu^{3+} and cation B = Gd^{3+} or Dy^{3+} and rearranged eq 1 to eq 2:

$$I_D(X_B/X_A) + 1 = 1/x_A \quad (2)$$

where $I_D = (P_B/P_A)$ = discrimination index of cation B over A for incorporation into the crystalline product.

Table 3. Temperature Evolution of Decay Rates[a] for $[\{Na\}\{(\mathbf{sal})_3Eu_xLn'_{1-x}(B(OMe)_4Eu_xLn'_{1-x}(\mathbf{sal})_3\}]_n$

	Ln =	Eu	Ln =	Gd[b]	Ln =	Y[c]	Ln =	Dy[d]	Ln =	Gd/Dy[e]
T (K)	k_1/s × 10^4	k_2/s × 10^3	k_1/s × 10^4	k_2/s × 10^3	k_1/s × 10^4	k_2/s × 10^3	k_1/s × 10^4	k_2/s × 10^3	k_1/s × 10^4	k_2/s × 10^3
8−50		2.2		2.2		2.2	1.0			
55		2.2								
60				2.2		2.2	1.0	3.1	1.1	3.4
65		2.2					1.0	3.2		
70						2.2				
75							*f*	3.3		
80				2.2					1.0	4.0
85		2.2				2.3				
100				2.2			1.1	3.6	1.1	4.0
105		2.2				2.3				
110				2.2						
120							1.1	3.7		
125		2.2				2.3				
140				2.3		2.3	1.2	4.0	1.1	4.1
145		2.2								
155						2.3				
160										
165				2.2		2.3	1.4	4.0		
180							*f*	4.1	1.2	5.5
185		2.2								
200				2.2			1.4	4.2		
205		2.2				2.4				
210										
215							1.5	4.3		
220		2.3		2.4		2.4			1.0	6.2
225		2.4				2.5				
235		2.5				2.7				
240		2.7		2.7		2.8	1.7	4.4		
245		3.0		3.0		2.9				
250	1.8	3.4		3.5		3.3	1.7	5.1		
255	*f*	3.8		3.7		3.5				
260	2.0	4.4		4.1	1.5	3.6	1.9	5.9	1.4	7.5
265	2.0	5.3		4.5	*f*	4.1				
270	*f*	6.3	1.7	5.1	1.8	4.2	2.0	6.5	1.6	7.9
275	2.3	7.4			2.2	5.5	2.5	7.7	2.5	8.8
280	2.5	9.1	2.4	5.8	2.5	5.7	*f*	8.7	2.4	7.9
285	2.4	11.1			3.3	7.4	3.0	10.4	3.0	8.8
290	3.4	13.2	2.9	10.4	3.4	7.2	3.6	12.0	3.4	9.9
295	4.5	17.5			5.0	11.8	5.9	15.2	3.7	10.5
297	6.7	16.7	4.3	10.0						
300	8.3	20.4					8.3	19.6	4.0	11.8
310	9.1	28.6								
320	14.3	40.0								

[a] Tails of decay curves were fit as single exponentials; the fast components were derived from double-exponential approximations. [b] $x = 0.06$. [c] $x = 0.04$. [d] $x = 0.58$. [e] $Gd_{0.29}Dy_{0.42}Eu_{0.29}$. [f] Nonlinear Marquardt fit not satisfactory.

derivatives were isolated.[19] The contrasting synthetic results of series **1** and **4** are intriguing. Experiments designed to determine the influence of thermodynamic and kinetic stabilities of corresponding Ln^{3+} coordination polyhedra as well as extended supramolecular interactions are in progress. This dearth of information notwithstanding, the consistent formation of complexes of **4** in high yield and over much of the lanthanide(III) series is very encouraging. Better understanding of the coordination behavior of $[(RO)_4B]^-$ anions and exploitation of their versatility as general synthons for one-dimensional materials should be of great future interest.

Luminescence Spectroscopy

Structurally, compounds of the $[\{Na\}\{(\mathbf{sal})_3Ln(B(OMe)_4)Ln(\mathbf{sal})_3\}]_n$ series are unequivocally one-dimensional. But the tight trough-into-crest crystal packing of the sinusoidal chains results in some interchain distances (shortest, 7.22 Å for **5**) that are comparable with the intrachain ones (longest, 6.84 Å for **5**). It was thus interesting to determine whether intrachain Ln^{3+}−Ln^{3+} electronic coupling resulting from through-bond interactions provides a better conduit for energy transfer than interchain electronic coupling facilitated by crystal packing forces and through-space interactions. Stronger intrachain coupling would constrain excitation energy transport in $[\{Na\}\{(\mathbf{sal})_3Ln(B(OMe)_4)Ln(\mathbf{sal})_3\}]_n$ to one dimension, otherwise multidimensional energy transport would dominate.[20] We thus studied in detail the luminescence spectral and decay dynamical properties of the emitting $[\{Na\}\{(\mathbf{sal})_3Eu(B(OMe)_4)Eu(\mathbf{sal})_3\}]_n$ (**5**) chains and their mixed metal analogues **7**−**19** (Table 1) to establish the nature and dynamics of electronic interactions in this structural motif.

The gadolinium(III) compound (**6**) shows broad ligand ($\mathbf{sal}^-$) absorptions that lead to complex emission (350−600 nm) (Figure 5) at both 297 and 77 K. This ligand emission overlaps

(19) Ephritikhine, M. *Chem. Rev.* **1997**, *97*, 2193.

(20) When energy transfer from a donor to an acceptor is predominantly multipolar,[21] the transfer rate (k) is expressed as:

$$k = C/R^n \qquad (3)$$

where C = multipolar coupling constant responsible for energy transfer; n = the order of the multipolar interaction (6, 8, or 10 for dipole−dipole, dipole−quadrupole, and quadrupole−quadrupole interactions, respectively), and R = metal−metal separation.

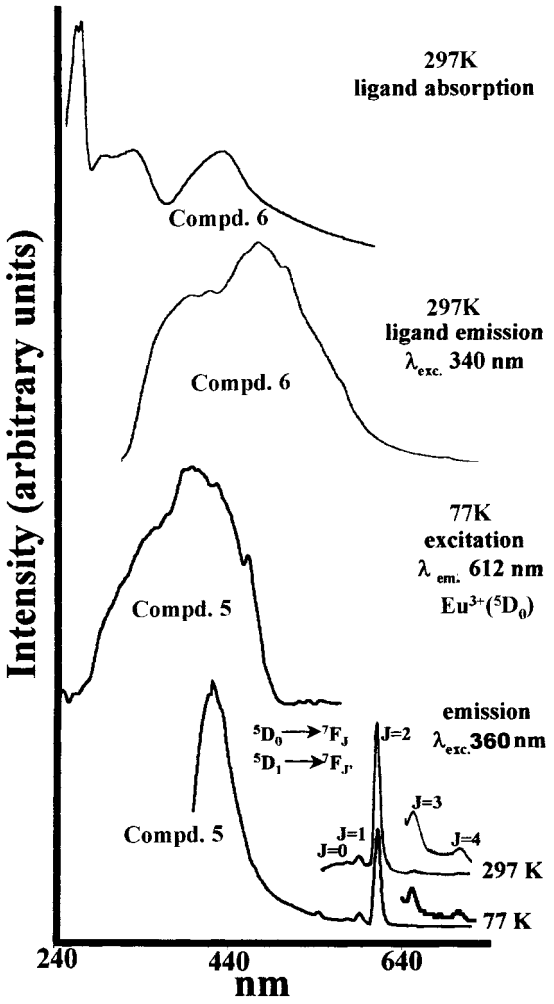

Figure 5. Electronic spectra for compounds **5** and **6**.

with electronic absorptions of luminescent Tb^{3+} and Eu^{3+} ions thereby meeting the principal Dexter−Förster condition[21] for ligand-to-metal energy transfer which may culminate in the 'antenna effect'. When excited in the ligand absorption region ($\lambda_{exc} = 360$ nm), the europium(III) complex (**5**) yields red Eu^{3+} ($^5D_0$) emission, albeit rather weak (Figure 5). The excitation spectra of Eu^{3+} ($^5D_0$) emission ($\lambda_{em} = 612$ nm) are dominated by ligand absorptions but very strange differences exist which depend on both temperature and europium(III) ion concentration (Figure 6). For example, at 297 K, the excitation spectrum of Eu^{3+} ($^5D_0$) emission ($\lambda_{em} = 612$ nm) from the pure europium(III) compound **5** features prominent direct Eu^{3+} $^5D_1 \leftarrow {}^7F_j$ ($j = 0, 1$) and weaker $^5D_2 \leftarrow {}^7F_j$ ($j = 0, 1$) transitions superimposed on a broad **sal**$^-$ absorption tail which extends into the green region ($\lambda > 480$ nm) (Figure 6, compound **5**). In sharp contrast to this behavior, the prominence of these direct europium(III) $^5D_{1,2} \leftarrow {}^7F_{0,1}$ transitions decreases systematically with decreasing concentration of europium(III) ions in crystals of the mixed $[\{Na\}\{(\mathbf{sal})_3Gd_{1-x}Eu_x(B(OMe)_4)Gd_{1-x}Eu_x(\mathbf{sal})_3\}]_n$ (**7**−**9**) (Figure 6). Concomitantly, the low-energy **sal**$^-$ green absorption tail takes on a systematic blue shift with decreasing europium(III) concentration and becomes insignificant at $\lambda \approx 480$ nm for compound **7** (Figure 6, compound **7**) where the Eu^{3+} concentration is the least. The 77 and 297 K excitation spectra of **7** and **12** (Figure 6) and that of **5** at 77 K (Figure 5) are similar. Further, the $^5D_0 \rightarrow {}^7F_j$ emission spectrum (Figure 5) is

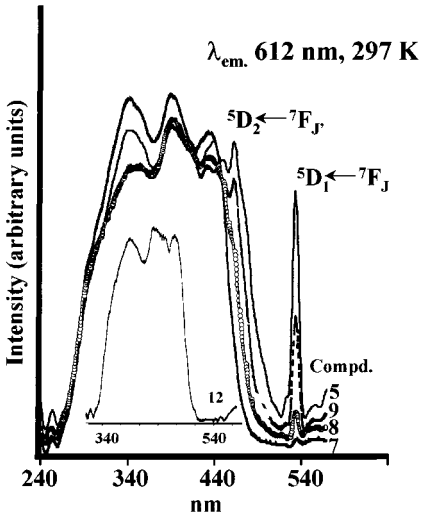

Figure 6. The 297 K excitation spectra for compounds **5**, **7**−**9**, and **12**.

dominated by the so-called hypersensitive[22] $^5D_0 \rightarrow {}^7F_2$ peak and, quite unusually, the forbidden $^5D_0 \rightarrow {}^7F_0$, $^7F_3$ transitions[23] are more intense than the allowed $^5D_0 \rightarrow {}^7F_4$ electric dipole. It seems that the geometrical disposition of the various oxygen atoms around the 8-fold coordinated Eu^{3+} ion produces an effective crystal electric field of very low symmetry; hence, the observed Eu^{3+} ($^5D_0$) emission spectral profile in the 580−630 nm region (Figure 5). However, symmetry and group theory arguments that allow for weak $^5D_0 \rightarrow {}^7F_3$ intensity do simultaneously predict greater probabilities for electric dipole $^5D_0 \rightarrow {}^7F_j$ ($j = 2, 4, 6$) transitions.[22]

Thus, arguments based on symmetry of the coordination polyhedron around Eu^{3+} and impurity emission cannot explain satisfactorily the unusual intensities of the $^5D_0 \rightarrow {}^7F_3$ transition.

To shed more light on the nature of the emitting europium(III) species and the energy-transport dynamics in the sinusoidal $[\{Na\}\{(\mathbf{sal})_3Ln(B(OMe)_4)Ln(\mathbf{sal})_3\}]_n$ chains, we studied the temperature evolution of the decay behavior of the resulting emission in detail and found that the luminescence decay kinetics fall into two regimes (Table 3): low ($8 < T < 220$ K) and high ($T > 220$ K) temperature.

Luminescence Decay Dynamics of Eu^{3+} ($^5D_0$) at Low Temperature ($T < 220$ K). Direct excitation of the Eu^{3+} ($^5D_0$) level at 572 nm in **7** and **12**, in which Eu^{3+} ions are well separated by the effectively inert Gd^{3+} and Y^{3+} ions, and in the pure europium compound **5** produces red emission that decays exponentially for $8 < T < 220$ K (Table 3). The spontaneous decay rate is ca. 2.2×10^3 s^{-1} whereas a weak temperature dependence corresponding to a phonon-type thermal barrier of ca. 100 cm^{-1} is observed. The 77 K decay curves of Eu^{3+} ($^5D_0$) emission from other mixed gadolinium(III)/europium(III) compounds **8**−**11** are also exponential with similar decay rates (2.2×10^3 s^{-1}). Indiscriminate (at 365 nm) and direct (at 510−535 nm) excitation of the Eu^{3+} ($^5D_1$) level in **5** produces an excitation buildup of ca. 7.7×10^5 s^{-1} which is of the same order of magnitude as the decay rate of the Eu^{3+} ($^5D_1$) emission (ca. 7.7×10^5 s^{-1}). This means that ligand-to-Eu^{3+} ($^5D_1$) energy transfer at low temperature is faster than the Eu^{3+} ($^5D_1$)-to-Eu^{3+} ($^5D_0$) energy transfer, and confirms the involvement of Eu^{3+} ($^5D_1$) in the sensitization of Eu^{3+} ($^5D_0$) emission that is inferable from the excitation spectra (Figures 5 and 6).

(21) (a)Dexter, D. L. *J. Chem. Phys.* **1953**, *21*, 836. (b) Förster, T. *Z. Naturforscher.* **1949**, *49*, 321.

(22) Försberg, J. H. *Coord. Chem. Rev.* **1973**, *10*, 195.

(23) (a) Blasse, G. *Inorg. Chim. Acta* **1988**, *142*, 153. (b) Thompson, L. C.; Kuo, S. C. *Inorg. Chim. Acta* **1988**, *149*, 305.

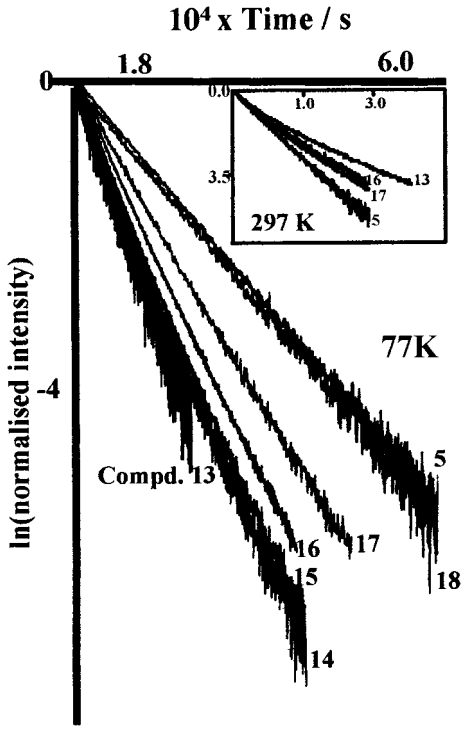

Figure 7. The 77 and 297 K (insert) decay curves (λ_{em} = 612 nm; λ_{exc} = 572 nm) of Eu^{3+} ($^5D_0$) in mixed metal europium/dysprosium compounds **5** and **13**−**18**.

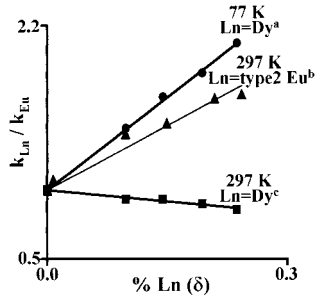

Figure 8. Stern−Volmer plots [ratio of decay rates vs mole fraction of Ln acceptor (δ) for the major Eu^{3+} ($^5D_0$) emission in mixed metal europium/dysprosium compounds **13**−**18**]. [a] $k_{Dy}/k_{Eu} = 1 + 4.54\ \delta_{Dy}$ [k_{Eu} = decay rate of Eu^{3+} ($^5D_0$) in **5** at 77 K; k_{Dy} = decay rate of Eu^{3+} ($^5D_0$) in the presence of Dy^{3+}]; [b] $k_{type2Eu}/k_{type1Eu} = 1 + 1.02\ \delta_{type2Eu}$ [$k_{type1Eu}$ = decay rate of Eu^{3+} ($^5D_0$) in **7** at 297 K; $\delta_{type2Eu} = \delta_{Eu}$ for comparative purposes; $k_{type2Eu}$ = decay rate of long-lived component of Eu^{3+} ($^5D_0$) in compounds **13**−**18** at 297 K]; [c] $k_{Dy}/k_{Eu} = 1 - 0.59\ \delta_{Dy}$ [k_{Eu} = decay rate of Eu^{3+} ($^5D_0$) in **5** at 297 K; $k_{type2Eu}$ = decay rate of long-lived component of Eu^{3+} ($^5D_0$) of compounds **13**−**18** at 297 K].

The exponential nature of decay curves of quenched Eu^{3+} ($^5D_0$) emission is indicative of efficient energy migration on the Eu^{3+} sublattice. To establish the dimensionality of this regime in crystals of $[\{Na\}\{(\mathbf{sal})_3Eu(B(OMe)_4)Eu(\mathbf{sal})_3\}]_n$, we studied the luminescence decay behavior of mixed Eu^{3+}/Dy^{3+} compounds **13**−**18** (Figure 7). Quenching of 77 K Eu^{3+} ($^5D_0$) emission by Dy^{3+} ions (compounds **13**−**18**) follows Stern−Volmer kinetics[24] (Figure 8; 77 K), the decay curves deviating marginally from single-exponential behavior throughout the entire concentration range of Dy^{3+} studied. This confirms that the energy-transport regime in **5** and **13**−**18** is dominated by efficient energy migration that culminates in less efficient quenching by traps (e.g., Dy^{3+}). $Eu^{3+}-Eu^{3+}$ interactions are therefore much stronger than the $Eu^{3+}-Dy^{3+}$ interactions, and

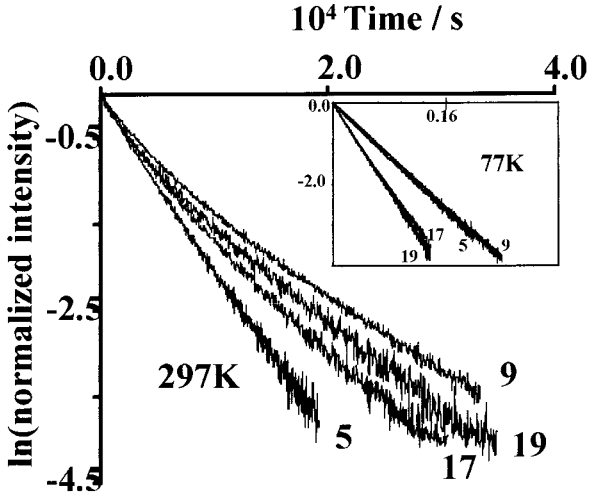

Figure 9. Decay curves of Eu^{3+} ($^5D_0$) emission (λ_{em} = 612 nm; λ_{exc} = 572 nm) in **5** and mixed metal compounds **9**, **17**, and **19**.

the energy-transport regime is nearly dynamic.[25,26] It is well known that introduction of energy scatterers into donor−acceptor arrays dominated by one-dimensional energy-migration regimes produces a dramatic effect on decay-curve profiles.[27,28] However, neither the decay curves of **17** and **19** nor those of **5** and **9** show the expected dramatic differences at 77 K (Figure 9 insert). This means that energy migration in $[\{Na\}\{(\mathbf{sal})_3Eu(B(OMe)_4)Eu(\mathbf{sal})_3\}]_n$ is multidimensional, and through-space multipolar $Eu^{3+}-Eu^{3+}$ interactions are more efficient conduits of excitation energy than through-bond interactions of the sinusoidal chains. The temperature evolution of luminescence decay rates of compounds **17** and **19** were very similar (Table 3); both exhibited weak temperature dependence for $50 < T < 220$ K with a phonon-type thermal barrier of roughly 40 cm^{-1}.

From the slope of the 77 K Stern−Volmer plot (Figure 8; 77 K), the limiting Eu^{3+} ($^5D_0$)-to-Dy^{3+} energy-transfer rate is ca. $9 \times 10^3\ s^{-1}$. This parameter is comparable with the value of ca. $6 \times 10^3\ s^{-1}$ obtained from perfectly exponential decay curves of Eu^{3+} ($^5D_0$) in compound **13**. Assuming that Eu^{3+} ($^5D_0$)-to-Dy^{3+} energy transfer is predominantly dipolar, the dipole−dipole coupling constant responsible for the transfer is ca. 4×10^{-52} $m^6\ s^{-1}$ which is reasonable.[26]

Luminescence Decay Dynamics of Eu^{3+} ($^5D_0$) at High Temperature ($T > 220$ K). After direct excitation at 572 nm, luminescence from isolated Eu^{3+} ($^5D_0$) states of compounds **7** and **12** decays exponentially for $220 < T < 260$ K. However, the decay behavior exhibits a strong temperature dependence throughout the $220 < T < 300$ K region and is not exponential for $T > 260$ K. For both **7** and **12**, the thermal barriers for quenching processes of the long- and short-lived red Eu^{3+} ($^5D_0$) emission (monitored at 612 nm) are ca. 2.1×10^3 (Figure 10) and 3.1×10^3 cm^{-1}, respectively. Eu^{3+} ($^5D_0$) emission decay behavior of crystalline **5** is similar to that of **7** and **12** up to 250 K. Thereafter, a stronger temperature dependence is observed with decay curves deviating very marginally from single exponential behavior (Figure 11) because of the appearance of a short-lived component (Table 3). The long-lived

(24) Zhou, Q.; Swager, T. M. *J. Am. Chem. Soc.* **1995**, *117*, 12593.

(25) (a) Huber, D. L. *Phys. Rev.* **1979**, *B20*, 2307. (b) Huber, D. L. *Phys. Rev.* **1979**, *B20*, 5333.

(26) Howell, R. C.; Spence, K. V. N.; Kahwa, I. A.; White, A. J. P.; Williams, D. J. *J. Chem. Soc., Dalton Trans.* **1996**, 961.

(27) Parkes, C. C.; Kahwa, I. A.; McPherson, G. L. *Phys. Rev.* **1995**, *52*, 11, 777.

(28) McPherson, G. L.; Waguespack, Y. Y.; Vanoy, T. C.; Rodriguez, W. J. *J. Chem. Phys.* **1990**, *92*, 1768.

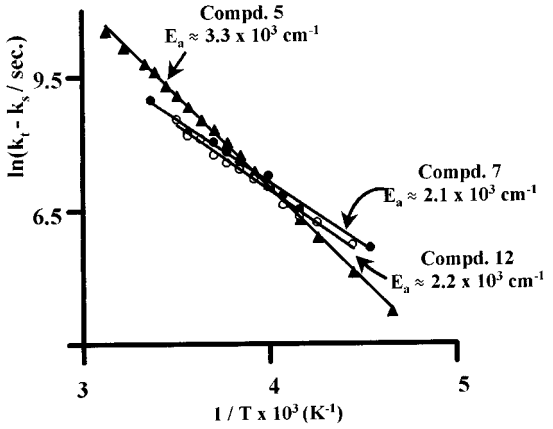

Figure 10. The temperature evolution of the trapping rates of the major (slowly decaying) Eu^{3+} ($^5D_0$) emission component for **5**, **7**, and **12** in the high-temperature regime ($210 < T < 300$ K). k_s = spontaneous decay rate = 2.2×10^3 s^{-1}; k_t = trapping rate = $k_o - k_s$ (k_o = observed rate).

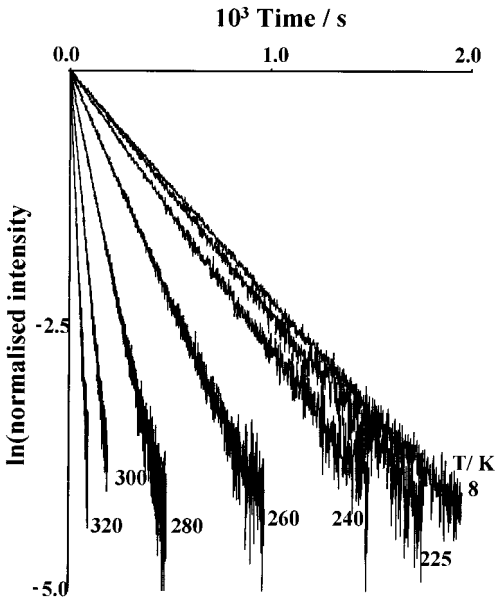

Figure 11. Temperature evolution of decay curves of Eu^{3+} ($^5D_0$) emission (λ_{em} = 612 nm; λ_{exc} = 572 nm) from **5** (8−320 K).

component decay is single exponential over six lifetimes. Thermally activated quenching of both the fast- and slow-decaying components require similar activation energies, ca. 3.1 $\times 10^3$ and 3.3×10^3 cm^{-1} (Figure 10), respectively. To shed more light on the nature of the thermally activated quenching process and its dependence on the nature of Ln in [{Na}-{(**sal**)$_3$Ln(B(OMe)$_4$)Ln(**sal**)$_3$}]$_n$ we studied the mixed compounds **13**−**18**. In sharp contrast to the behavior at 77 K, the 297 K decay curves of Eu^{3+} ($^5D_0$) emission from mixed dysprosium/europium compounds **13**−**18** (Figure 7, insert) are not single exponential and have initial slopes similar to that of **5**; but those compounds with the most dysprosium traps have the most intense Eu^{3+} ($^5D_0$) emission (Figure 7, insert). As a result, the long-lived component of Eu^{3+} ($^5D_0$) emission from compounds **5** and **13**−**18** at 297 K exhibits an extraordinary anti-Stern−Volmer dependence on the concentration of Dy^{3+} (Figure 8). This anomaly is corroborated by the comparative luminescence decay behavior of **5**, **9**, **17**, and **19** (Figure 9) in which the initial decay rates are of similar magnitude, and the tail decay rates are in the unexpected order of **9** < **19** < **17** < **5**. The activation energy for thermally activated quenching of the short- and long-lived Eu^{3+} ($^5D_0$) emission from **17** (220 < T < 300 K) are very similar to those of **5** (ca. 3×10^3 cm^{-1}). That of **19** (ca. 1.6×10^3 cm^{-1}) is more similar to those of **7** and **12** (ca. 2.1×10^3 cm^{-1}).

To explain the above-mentioned results, we propose that there are two types of Eu^{3+} ions in [{Na}{(**sal**)$_3$Eu(B(OMe)$_4$)Eu-(**sal**)$_3$}]$_n$ (**5**) chains. **Type 1 Eu^{3+}** occupies the regular europium-(III) sites in chains of **5** as shown in Figure 3 and is responsible for the Eu^{3+} ($^5D_0$) excitation profile exhibited by compounds **5** at 77 K (Figure 5) as well as **7** and **12** at 297 K (Figure 6). **Type 2 Eu^{3+}** sites are crystal defects, the population of which increases with the concentration of europium in compounds **5**−**12** and **13**−**19**. These defect sites would in this case be responsible for the dominant $^5D_{1,2} \leftarrow {}^7F_{0,1}$ transitions and the green absorption tail ($\lambda > 480$ nm) seen in Figure 6 (compounds **5** and **7**−**9**). There is good spectral overlap between the broad 500−600 nm emission tail (Figure 5) and the Eu^{3+} $^5D_{0,1,2} \leftarrow {}^7F_{0,1}$ absorptions (Figure 6); hence, the strong absorption tail at 480 nm in the excitation spectra (Figure 6) is most likely associated with the defect site. Most probably **Type 2 Eu^{3+}** arises from swapping Eu^{3+} and Na^+ sites, which is reasonable, in view of similarities in their cationic radii (ca. 1 Å for 6-fold coordination).[17] It is unlikely that the defect **Type 2 Eu^{3+}** site is a hydrate, because samples prepared from deuterated solvents (CH_3OD and D_2O) did not exhibit the dramatic decrease in luminescence decay rates usually seen when coordinated H_2O is replaced by D_2O.[9b,29] Instead, differences in **Type 1** and defect **Type 2** sites are expected to arise from the differential in site symmetry (at most D_{4d} and ca. O_h, respectively) and the nature of coordinated atoms (vide supra). The main Eu^{3+} ($^5D_0$) emission in **5** is caused by **Type 1 Eu^{3+}** and is sensitized as well as quenched via back energy transfer by thermally activated processes involving both the ligand absorption (at 480 nm) and **Type 2 Eu^{3+}**. This explains well the excitation spectral features (Figure 6, compounds **5** and **7**−**9**) and the thermally activated quenching processes (Figure 11 and Table 3) as well as their dependence on the concentration of europium(III). For comparative purposes, when a simple proportionality between the population of **Type 2 Eu^{3+}** and the europium concentration in the crystals is assumed and the Stern−Volmer plot revised accordingly, the normal profile is obtained (Figure 8).

Within this scheme, the short-lived component may be attributed to direct **Type 1 Eu^{3+}**-to-**Type 2 Eu^{3+}** energy transfer, the moderate efficiency of which precludes complete homogenization of the europium ion population by energy migration. The thermal barriers of about 2×10^3 and 3×10^3 cm^{-1} correspond to the energies required to bridge the Eu^{3+} ($^5D_0$) with the upper Eu^{3+} ($^5D_1$) and the ligand state responsible for the absorption at 480 nm, respectively. Most likely, back energy transfer to the ligand states associated with the **Type 2 Eu^{3+}** site predominantly quenches Eu^{3+} ($^5D_0$) emission from compounds rich in Eu^{3+}. Transiting the Eu^{3+} ($^5D_1$) state may be essential for quenching of Eu^{3+} ($^5D_0$) emission for compounds with too few **Type 2 Eu^{3+}**sites such as **7**, **12**, and **19**. It is remarkable that the green tail overlaps well with the Tb^{3+} ($^5D_4$) state; this may be the reason for efficient quenching of terbium-(III) emission from compound [{Na}{(**sal**)$_3$Tb(B(OMe)$_4$)Tb-(**sal**)$_3$}]$_n$.[30]

General Remarks

We have shown conclusively how hitherto elusive one-dimensional Ln^{3+} compounds of the $[(CH_3O)_4B]^-$ chelate can

(29) Horrocks, W. DeW.; Sudnick, D. R. *J. Am. Chem. Soc.* **1979**, *101*, 334.
(30) Piguet, C.; Bünzli, J.-C. G.; Bernardinelli, G.; Hopfgartner, G.; Petoud, S.; Shaad, O. *J. Am. Chem. Soc.* **1996**, *28*, 6681.

be prepared consistently and throughout much of the lanthanide series. The formation of both linear (**1**) and sinusoidal (**4**−**19**) systems suggests that a variety of one-dimensional motifs may be accessible through use of the $[(CH_3O)_4B]^-$ chelate to bridge Ln^{3+} ions. The challenge seems to be finding suitable complementary counteranions to stabilize one-dimensional compounds of desired Ln^{3+} ions. The luminescence spectra and energy-transport dynamics exhibited by compounds **4**−**19**, especially the dominance of through-space against through-bond Eu^{3+}−Eu^{3+} electronic interactions, are intriguing and require better understanding. For these reasons and the extended structural elegance of **1**, **2**, and **4**−**19**, further synthetic and luminescence work is in progress.

Acknowledgment. We thank the University of the West Indies (UWI) and the Government of St. Lucia for a scholarship to Alison Gajadhar-Plummer, and the UWI/Inter-American Development Bank (IDB) development program (R&D Project no. 29) for financial support. We also thank the British-Council/UWI CICHE Program for supporting the UWI-Imperial College collaboration, and we thank the staff of the International Center for Environment and Nuclear Sciences (nuclear activation analyses), The Jamaica Bauxite Institute (powder X-ray diffraction) and Tropical Metabolism Research Unit (UWI) (Perkin-Elmer LS5B spectrometer) for assistance with analyses.

Supporting Information Available: Tables S1−S11 lists elemental analyses for **4**−**19**, atomic positions, bond angles and distances, anisotropic displacement parameters, and hydrogen coordinates for **4** (Ln = Nd) and **5**; Figure S1 shows the stereoscopic view of **5**; Figure S2 shows the ORTEP diagram of **4** (Ln = Nd). This material is available free of charge via the Internet at http://pubs.acs.org.

IC9810788